

UCLA

UCLA Previously Published Works

Title

Differential electron yield imaging with STXM

Permalink

<https://escholarship.org/uc/item/8kd1165x>

Authors

Hubbard, William A

Lodico, Jared J

Ling, Xin Yi

et al.

Publication Date

2021-03-01

DOI

10.1016/j.ultramic.2020.113198

Peer reviewed

Differential electron yield imaging with STXM

William A. Hubbard^{1,2}, Jared J. Lodico^{1,2}, Xin Yi Ling^{1,2}, Brian Zutter^{1,2}, Young-Sang Yu³, David Shapiro³, B. C. Regan^{1,2}

¹*Department of Physics and Astronomy, University of California, Los Angeles, CA 90095, U.S.A.*

²*California NanoSystems Institute, University of California, Los Angeles, CA 90095, U.S.A.*

³*Advanced Light Source, Lawrence Berkeley National Laboratory, Berkeley, CA, 94720, U.S.A.*

Abstract

Total electron yield (TEY) imaging is an established scanning transmission X-ray microscopy (STXM) technique that gives varying contrast based on a sample's geometry, elemental composition, and electrical conductivity. However, the TEY-STXM signal is determined solely by the electrons that the beam ejects from the sample. A related technique, X-ray beam-induced current (XBIC) imaging, is sensitive to electrons and holes independently, but requires electric fields in the sample. Here we report that multi-electrode devices can be wired to produce differential electron yield (DEY) contrast, which is also independently sensitive to electrons and holes, but does not require an electric field. Depending on whether the region illuminated by the focused STXM beam is better connected to one electrode or another, the DEY-STXM contrast changes sign. DEY-STXM images thus provide a vivid map of a device's connectivity landscape, which can be key to understanding device function and failure. To demonstrate an application in the area of failure analysis, we image a 100 nm, lithographically-defined aluminum nanowire that has failed after being stressed with a large current density.

Keywords: STXM, TEY, XBIC, scanning transmission X-ray microscopy, electron yield, failure analysis

1. Introduction

In scanning transmission X-ray microscopy (STXM), a focused X-ray beam is rastered across a thin sample, and the measured transmission is associated with the beam position to form an image. With soft (100–2,200 eV) X-rays, STXM offers distinct advantages over other spectromicroscopy techniques. Its sub-50 nm [1, 2, 3] spatial resolution is better than the $\sim 1\ \mu\text{m}$ resolution of Raman imaging, and its beam-induced radiation damage is less than that of electron energy loss spectroscopy (EELS) in a transmission electron microscope (TEM) [4, 5]. STXM has found broad application in the biological [3, 6, 7] and physical [8, 9, 10] sciences, and has been used to study device physics in solar cells [11, 12], spin-torque memory [13], resistive memory [14], and the Li-ion battery cathode material Li_xFePO_4 [15].

STXM characterizes physical structure: it deter-

mines a sample's morphology and can even spectroscopically quantify a sample's chemical composition. However, in some cases the information returned is still too crude to identify gross characteristics of the sample that are of paramount importance. For instance, in an electronic device two conductors might be separated by a few nanometers of insulator. Conventional STXM might identify copper on one side and aluminum on the other, but, with its limited spatial resolution, conventional STXM is ill-suited to determine whether the two conductors are electrically connected. Because of the intimate relation between connectivity and function in electronic devices, determining the presence (or absence) and properties of such a connection might be the primary motivation for imaging the sample in the first place.

A conventional STXM system detects the transmitted X-rays with, for example, a photodiode on the beam-exit side of the sample. To expand its ca-

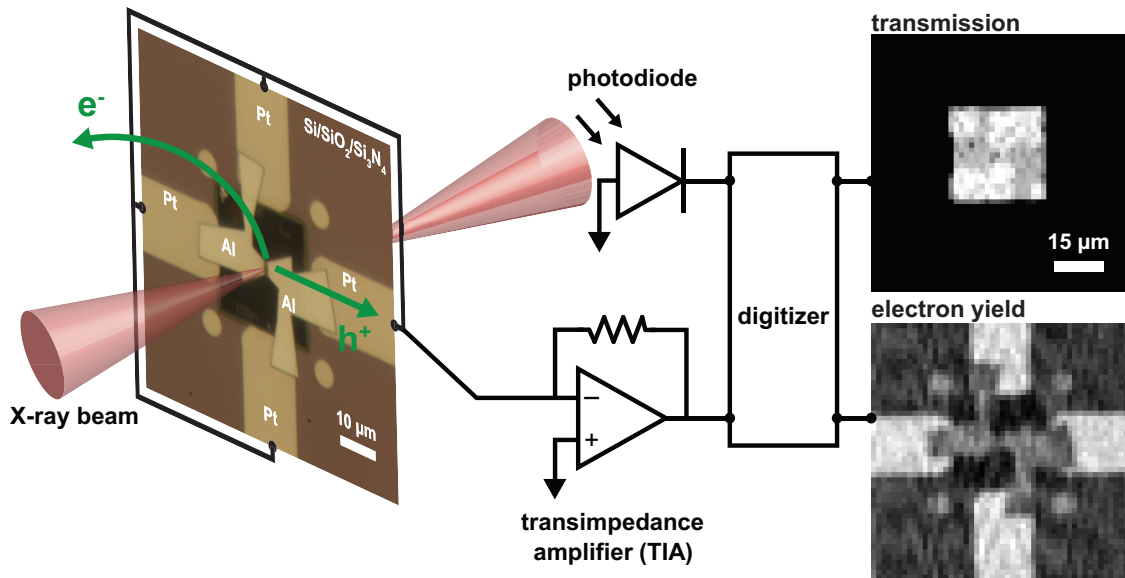


Figure 1: **Experiment overview.** The sample (optical image on left) consists of a $200\ \mu\text{m}$ -thick silicon chip supporting a $20\ \text{nm}$ -thick silicon nitride membrane. Platinum leads over the silicon contact an aluminum pattern that tapers to an unresolved wire in the membrane's center. Here all of the Pt leads are shorted together to produce a TEY image. As the X-ray beam (red) scans the sample, the signal from the photodiode and the transimpedance amplifier (i.e. TIA, or current meter) are digitized simultaneously to form the images on the right. The photodiode signal generates the standard STXM image (top right). The TIA measures the current produced in the sample by the X-ray beam (bottom right). When the beam ejects electrons from the sample, the resulting hole current is positive and is displayed with bright contrast.

40 pabilities, STXM imaging techniques that instead
 41 rely on electron detection have been developed.
 42 Among the most prominent are total electron yield
 43 (TEY) and X-ray beam-induced current (XBIC)
 44 imaging. TEY is performed either by capturing
 45 electrons emitted from the sample in a remote elec-
 46 tron detector [16, 1], or by measuring the resulting
 47 holes with a current meter attached to the sample
 48 [17, 1]. TEY measures beam-ejected electrons of all
 49 energies, including primary¹, secondary, and Auger
 50 electrons[18]. XBIC, on the other hand, requires
 51 a current meter attached to the sample. It mea-
 52 sures the current generated when the X-ray beam
 53 produces electron-hole pairs that are subsequently
 54 separated by local electric fields inside the sample
 55 [11, 12, 19, 20]. Generally XBIC signals, where
 56 present, are larger than TEY signals, because more
 57 electron-hole pairs than ejected electrons are pro-
 58 duced per primary X-ray.

¹In the X-ray microscopy community a primary electron is one scattered in a collision with beam X-ray, while in the electron microscopy community a primary electron is a beam electron, and a secondary electron is one scattered by a primary. In this article we use the conventions of the X-ray community.

59 XBIC has an electron microscopy counterpart,
 60 (standard) electron beam-induced current (EBIC)
 61 imaging, where the electron-hole pairs are instead
 62 produced by a scanned electron beam [21, 22]. A
 63 related electron microscopy technique, secondary
 64 electron emission EBIC (SEEBIC) imaging [23, 24,
 65 25], is closely analogous to TEY, and to the subject
 66 of this paper.

67 If the sample is wired for current collection, both
 68 TEY and XBIC imaging can be performed using the
 69 same apparatus, but with slightly different electri-
 70 cal connections. TEY requires only a single con-
 71 nection between the sample and the current meter
 72 (generally a transimpedance amplifier, or TIA)[19],
 73 while XBIC requires that the sample have an addi-
 74 tional connection to a low impedance to allow for
 75 charge neutralization.

76 Using a sample wired with multiple electrical con-
 77 nections, as is characteristic of XBIC and not TEY,
 78 we perform STXM mapping of electron yield. How-
 79 ever, the resulting contrast has its root in the ejection
 80 of electrons from the sample (and not in the crea-
 81 tion of electron-hole pairs), as is characteristic
 82 of TEY and not XBIC. Here we report that using

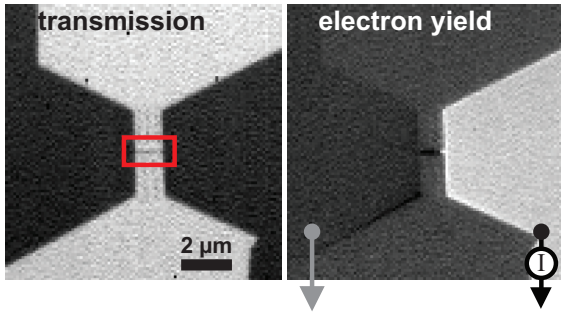


Figure 2: **STXM and DEY imaging of the Al nanowire device.** These images of the device of Fig. 1 are acquired with the left electrode grounded and the right electrode attached to the TIA (indicated schematically here with an “I” circumscribed by a circle). The field of view in these images corresponds to the x-ray transparent center of the Fig. 1 images, where the photodiode signal is bright. The standard STXM image (left) shows both Al leads with the same contrast, while the DEY image (right) indicates that only the Al lead on the right is electrically connected to the TIA. The red box indicates the region shown in Fig. 3.

multiple electrodes allows differential electron yield (DEY) imaging, which gives contrast that changes sign between neighboring electrodes on the sample. For instance, when the X-ray beam is incident on an electrode connected to the current meter, the measured current is generally positive, since the ejected electrons leave a hole current behind. But when the beam moves to a neighboring, grounded electrode, the beam-induced hole current is shunted to ground and is therefore not measured. Meanwhile, some of the primary and secondary electrons ultimately return to the first electrode, where they are measured as a negative current (analogous to Fig. 2 of reference [23]). This negative current represents electrons that, in the absence of the current meter, would *not* have left the sample, thus by definition it is distinct from the TEY current. The resulting DEY contrast, unlike standard STXM, TEY, or XBIC contrast, can vividly reveal whether neighboring electrodes are connected.

Our implementation of DEY imaging employs a TEM sample holder, which has some particular advantages for *in situ* STXM imaging of electronic devices. The production of STXM-compatible, electrically connected samples shares many challenges with the production of samples for *in situ* TEM experiments. Accordingly, several X-ray beamlines have incorporated TEM stage/load-lock mechanisms in X-ray imaging systems, allowing for STXM experiments to be performed with TEM

sample holders[26, 15, 27]. We adopt this approach [27], which gives access to the numerous off-the-shelf *in situ* capabilities afforded by specialized TEM holders, including imaging in liquid and gas, heating, cooling, biasing, and physical manipulation. The TEM stage and load-lock combination also makes for faster sample exchange (minutes instead of hours) and easier correlative TEM imaging (which can be performed without even removing the sample from the TEM sample holder).

2. Experimental

X-ray imaging is performed at Lawrence Berkeley National Lab’s Advanced Light Source (ALS) on beamline 7.0.1.2 (COSMIC) [27]. The COSMIC beamline offers a 250–2500 eV X-ray energy range and a 50 nm spot size, and is equipped with a FEI CompuStage load-lock system, which accepts TEM sample holders. Except where indicated otherwise, STXM images are acquired with an incident beam energy of 1565 eV. To form STXM and electron yield images, the signals from a post-sample photodiode and a FEMTO DLPCA-200 TIA, respectively, are digitized simultaneously as the beam is rastered pixel-by-pixel across the sample. To acquire diffraction patterns for ptychography, the photodiode can be retracted to expose a CCD detector [28]. Data are reconstructed using standard methods available in the SHARP ptychography package [29]. Scanning TEM (STEM) imaging is performed in an FEI Titan 80–300 STEM at 80 kV. For both STXM and STEM the sample is mechanically supported and electrically contacted with a Hummingbird Scientific biasing TEM sample holder.

Our demonstration sample (Fig. 1 optical image) is a silicon chip patterned via optical lithography with four Ti/Pt (5/25 nm) electrodes that lead to a 20 nm-thick silicon nitride membrane[23]. On the membrane a 1- μ m-long, 100-nm-wide, and 100-nm-thick Al wire is patterned via electron beam lithography. Tapered pads connect the wire to the Ti/Pt electrodes in a 4-wire configuration. Before being loaded in the STXM chamber, the wire is biased in vacuum until failure and then stored in the ambient atmosphere for several days. All images labeled “transmission” show the raw, unprocessed photodiode signal. All images labeled “electron yield” show the TIA signal, which has been Fourier filtered to remove AC line noise. TIA current values are given relative to the signal on the bare sil-

163 icon nitride membrane, where very little electron
 164 yield is expected. The optical density referenced
 165 in Figs. 5–6 is $-\ln \frac{I}{I_0}$, where I_0 is the photodiode
 166 signal on the bare silicon nitride membrane.

167 3. Results and Discussion

168 STXM imaging of the silicon nitride membrane
 169 window reveals the Al electrodes, which transmit
 170 fewer photons than the bare membrane and thus ap-
 171 pear slightly darker (Fig. 1 top right). But STXM
 172 imaging of the silicon support frame provides no in-
 173 formation, as the thick silicon blocks the incident
 174 X-rays. The (total) electron yield image, on the
 175 other hand, reveals device features in the entire field
 176 of view, even where the sample is opaque (Fig. 1
 177 bottom right). The Al pads are visible, as in the
 178 STXM image, but so are the Pt electrodes to which
 179 the Al is connected. The Pt has a larger electron
 180 yield than the Al and therefore appears brighter.
 181 Four Pt islands at the corners of the membrane are
 182 also visible, despite the apparent lack of an electri-
 183 cal connection. Holes produced in these islands can
 184 evidently travel the several-micrometer distance to
 185 the Pt electrodes [23]. Contrast is slightly darker
 186 over the membrane, an insulator that generates few
 187 primary electrons in the beam.

188 Electron yield mapping can be extremely help-
 189 ful in samples that are mostly opaque. With only
 190 the transmission-based contrast of standard STXM,
 191 locating a thin region is generally accomplished
 192 by trial-and-error, and is analogous to wandering
 193 around in the dark. Electron yield imaging turns
 194 the lights on: sample features far from the trans-
 195 parent area can be used as landmarks to locate the
 196 region of interest systematically and quickly.

197 The device of Fig. 1 features an unresolved Al
 198 wire that previously connected the two larger pads.
 199 Because the device has been subjected to a bias cur-
 200 rent sufficiently large to cause heating and eventual
 201 failure, the wire is broken and represents a very
 202 large electrical impedance. We image the nanowire
 203 of Fig. 1 again, this time with a smaller field of view
 204 (Fig. 2), but here we change the electrical connec-
 205 tions for DEY imaging: the right Al electrode re-
 206 mains connected to the TIA but the left electrode
 207 is now grounded. (The biasing sample holder gives
 208 independent access to each of the four Ti/Pt elec-
 209 trodes, so this change can be made without break-
 210 ing vacuum.)

211 In this configuration, when the X-ray beam ejects
 212 electrons from the right electrode, the TIA mea-

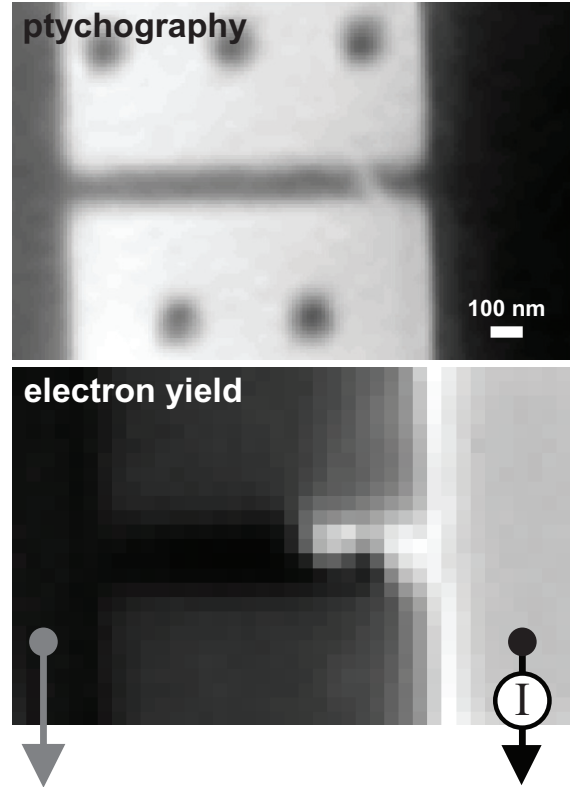


Figure 3: **Ptychography and DEY imaging of the Al nanowire device.** Retracting the photodiode and scanning over the region outlined in red in Fig. 2 produces, after reconstruction, a ptychography image (top) that reveals the break in the Al nanowire. The simultaneously acquired electron yield image (bottom) has the inferior resolution, relative to ptychography, of standard STXM, but it nonetheless reveals a surprising feature: electrical connectivity spans the ‘break’ in the Al wire that is seen in ptychographic image.

213 sures a positive (hole) current. When the X-ray
 214 beam ejects electrons from the left electrode, the
 215 hole current flows to ground directly and is not
 216 measured by the TIA. However, a fraction of the
 217 electrons emitted from the left electrode are recap-
 218 tured[23] by the right electrode and are measured
 219 as a negative (electron) current. Thus, the result-
 220 ing image (Fig. 2 right) shows each electrode as
 221 bright or dark respectively, depending on whether
 222 or not the electrode is directly connected to the
 223 TIA. Like TEY, DEY imaging maps whether or not
 224 a region is conducting: the Al on both sides of
 225 the break more readily emits primary electrons
 226 than the insulating Si_3N_4 support membrane. But
 227 DEY imaging also indicates the connectivity land-
 228 scape, particularly the ‘watershed’ boundary of the region electri-

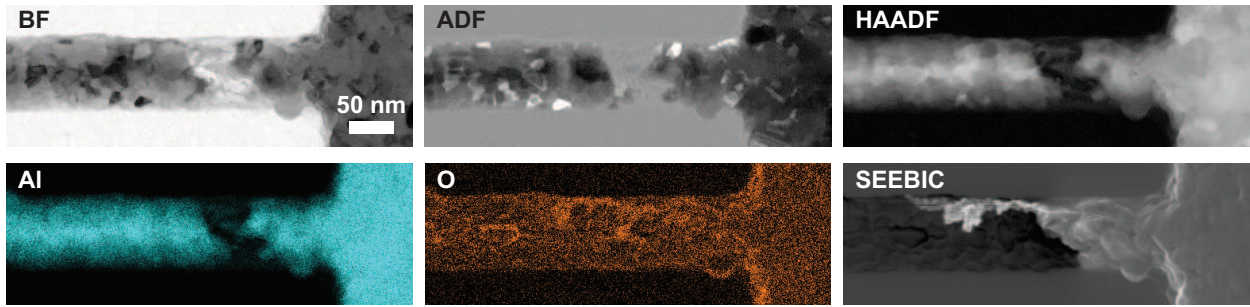


Figure 4: **STEM imaging of the Al nanowire device.** The Al wire of Figs. 1–3 is imaged with standard STEM (BF, ADF, and HAADF), STEM EDS elemental mapping (Al and O), and STEM SEEBIC. The BF and SEEBIC images are the electron microscopy analogues of the previously-shown STXM (Fig. 2) and DEY images (Figs. 2–3) respectively. The STEM images show similar contrast but significantly better spatial resolution relative to their analogous X-ray images.

229 cally connected to the TIA [23]. Such differential 264
 230 contrast is not accessible with TEY. 265

231 Note that the dark contrast generated by electron 266
 232 recapture (e.g. the left electrode of Fig. 2 right) 267
 233 indicates that DEY imaging, on electrodes showing 268
 234 bright contrast (e.g. the right electrode of Fig. 2 269
 235 right), always has a better signal-to-noise ratio than 270
 236 TEY imaging. The recaptured electron current has 271
 237 the opposite sign as the hole current. To the extent 272
 238 that these currents are equal and are collected 273
 239 by the same TIA, they cancel. Viewed from this 274
 240 perspective, TEY is a worst case scenario, in that 275
 241 the recapturing electrode spans the whole sample. 276
 242 It thus collects a correspondingly large recapture 277
 243 current, and generates a correspondingly small net 278
 244 current (i.e. signal). One can even imagine patho- 279
 245 logical geometries where a nearby, off-sample sur- 280
 246 face, such as an aperture [17], could produce enough 281
 247 primary and secondary electrons — which contain 282
 248 no information about the sample itself — to over- 283
 249whelm the original hole current. Imaging a small 284
 250 electrode that alone is connected to the TIA gives 285
 251 the best case scenario, for here the recapture cur- 286
 252 rent is minimized and the measured hole current is 287
 253 undiminished.

254 Scans of the same device (Fig. 3) with even 288
 255 smaller fields of view (i.e. higher magnification) re- 289
 256 solve both the physical and the electronic break in 290
 257 the Al wire. Here we retract the photodiode to cap- 291
 258 ture the diffraction pattern generated at each X-ray 292
 259 beam position (i.e. pixel) for ptychography. With- 293
 260 out the photodiode the standard STXM image is no 294
 261 longer available. Ptychographically reconstructing 295
 262 the captured diffraction patterns produces an image 296
 263 that reveals a break in the Al on the right side 297
 298

of the wire (Fig. 3 top). The break appears clean, 264
 with an ~ 50 nm length missing from the wire. The 265
 DEY image (Fig. 3 bottom), however, shows a more 266
 complicated structure around the break. The large 267
 Al lead on the right is bright, as expected based 268
 on the larger field of view (i.e. lower magnification) 269
 image of the same device (Fig. 2 right). But surpris- 270
 ingly, portions of the wire to the left of the ‘break’ 271
 (as identified by the ptychographic image) are also 272
 bright, indicating that they too are connected to 273
 the Al lead on the right. 274

275 During ptychographic imaging, the photodiode is 276
 retracted and thus its signal is not available. How- 277
 ever, electron yield data can still be acquired si- 278
 multaneously with the diffraction patterns used to 279
 produce the ptychographic image. And unlike the 280
 ptychographic data, the electron yield data is im- 281
 mediately viewable in a real-space format without 282
 any analysis (e.g. reconstruction or summing). The 283
 real-time feedback provided by electron yield imag- 284
 ing, like the ability to image opaque regions of a 285
 sample, is an experimental convenience that can 286
 save valuable time on the beamline.

287 The use of the TEM sample holder for X-ray 288
 289 imaging makes correlative microscopy especially 290
 straightforward. STEM (Fig. 4) imaging of the 291
 same device in the same sample holder confirms, 292
 with much improved spatial resolution, the device 293
 properties ascertained with X-ray imaging. Bright- 294
 field (BF), annular dark-field (ADF), and high- 295
 angle ADF (HAADF) STEM images (Fig. 4, top 296
 row) each show loss of material at the failure point, 297
 and energy-dispersive X-ray spectroscopy (EDS) el- 298
 emental mapping (Fig. 4, bottom left and center)

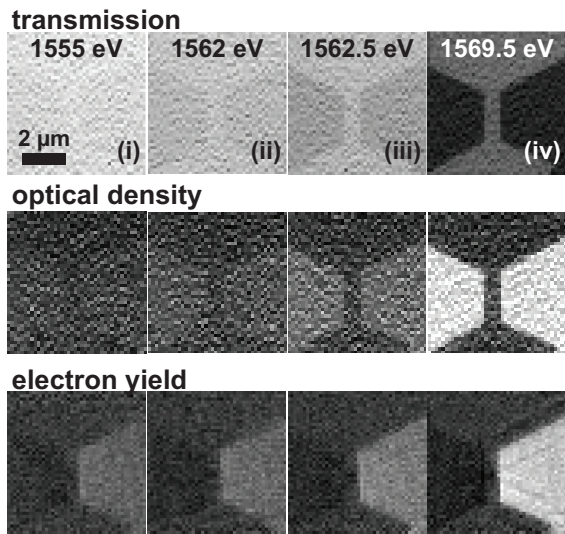


Figure 5: **STXM and electron yield images at four representative X-ray beam energies.** The beam energy for each column of representative images (see Fig. 6) is indicated. The electrodes are almost invisible in the raw photodiode (upper row) and calculated optical density (middle row) images below 1562 eV, while they are easily seen in the electron yield images (bottom row) over the entire energy range scanned (1555–1575 eV). The electron yield images are acquired with the circuit as indicated in Figs. 2–3. The contrast scale is held fixed for each row of images.

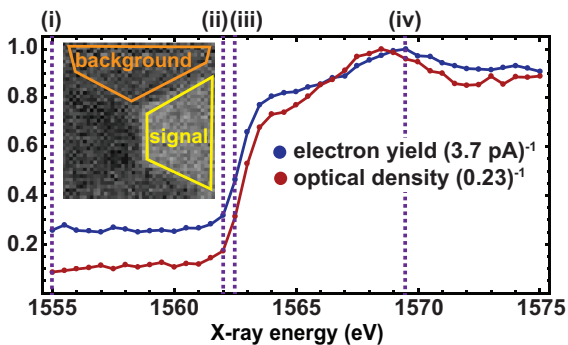


Figure 6: **Electron yield and optical density of an Al electrode as a function of incident beam energy.** Signal on the right electrode (inset, yellow) is plotted for the electron yield (blue curve) and optical density (red curve). Electron yield is measured relative to the background reference region (inset, orange). Both plots are normalized by dividing by the maximum value measured for each, which is indicated in the plot legend. Dashed lines indicate images shown in Fig. 5.

299 BIC imaging (Fig. 4, bottom right) shows the same
 300 non-obvious electrical connectivity seen with DEY
 301 imaging, again with improved spatial resolution:
 302 the right electrode is electrically connected to material
 303 well to the left of the gap that appears in the
 304 standard imaging channels. Both the DEY and the
 305 SEEBIC [23] images are mapping the connectivity
 306 landscape as revealed by beam-induced ejection of
 307 electrons from the sample. Evidently the contrast
 308 is relatively insensitive to the type of probe beam
 309 (X-ray or electron) and is thus predominantly determined
 310 by the sample’s conductivity distribution. While here
 311 electron microscopy has clearly superior spatial
 312 resolution, X-ray microscopy has spectroscopic
 313 advantages that will be discussed shortly.

314 Metallic aluminum in quantities below the detection
 315 limits here is likely responsible for this connectivity
 316 extension. Some correlation between the connectivity
 317 extension seen with DEY and SEEBIC imaging is seen
 318 in the oxygen EDS map, but nothing that would suggest
 319 the existence of the extension without the DEY (or
 320 SEEBIC) data. In many practical situations, DEY
 321 imaging’s ability to detect the electrical connectivity
 322 created by dopants or other trace impurities in
 323 quantities below the standard detection methods’
 324 thresholds might be key to understanding device
 325 behavior.

326 In X-ray microscopy, unlike electron microscopy,
 327 the beam energy can be tuned across an absorption
 328 threshold of an element in the sample. (This
 329 capability has been exploited in previous XBIC work
 330 [20].) The differential contrast in the electron
 331 yield persists under such spectroscopic imaging. We
 332 scan the beam energy over 41 values encompassing
 333 the aluminum K-edge (1555 eV to 1575 eV in 0.5
 334 eV steps). Below 1562 eV, the Al electrodes are
 335 difficult to detect in the STXM images, while they
 336 are obvious in the electron yield images (Fig. 5).
 337 Both signals become more intense (Fig. 6) as the
 338 energy exceeds the Al K-edge threshold at ~ 1563
 339 eV. The Al electron yield, which is already
 340 significant below the K-edge, increases by about
 341 400% immediately above the K-edge.

342 Spectroscopic tuning of an X-ray beam may give
 343 DEY imaging an important advantage over SEEBIC
 344 imaging for the study of chemically heterogeneous
 345 samples. Figure 6 shows clear evidence of X-ray
 346 absorption fine structure (XAFS) in the DEY
 347 signal, as has been seen previously in the TEY
 348 signal [16, 1]. With the ability to spectroscopically
 349 vary the electron yield according to elemental
 350 identity, molecular bonding, local disorder, and ef-

fective atomic charge, DEY imaging has the potential to directly relate the local chemistry to electrical transport properties, and thus give new insight into electrochemical systems ranging from batteries to doped semiconductors.

4. Conclusion

We have demonstrated STXM electron yield imaging of a simple device mounted in a TEM biasing holder. With a TEM load-lock installed, performing electron yield measurements requires no modification of the STXM chamber or the data acquisition electronics; all electrical connections to the device are made through the holder, and the electron yield signal is digitized in parallel with the existing photodiode signal. Measuring current from the entire device provides the standard TEY measurement, while grounding portions of the circuit gives DEY images that map connectivity within the device. In a broken Al nanowire, the differential contrast provided by DEY imaging precisely locates the failure point and reveals a non-obvious electrical connection spanning the physical gap in the wire. As a complement to standard STXM and ptychographic imaging, the DEY technique has a number of practical advantages, including real-time and opaque-region imaging. For functional studies of micro- and nano-scale electronic devices, DEY imaging makes a particularly powerful addition to the suite of available correlative imaging modes.

5. Acknowledgments

This work was supported by National Science Foundation (NSF) Science and Technology Center (STC) award DMR-1548924 (STROBE), by NSF award DMR-1611036, and by the UCLA PSEIF. Work at the ALS was supported by the Office of Science, Office of Basic Energy Sciences, of the US Department of Energy under contract number DE-AC02-05CH11231. The authors acknowledge the use of instruments at the Electron Imaging Center for NanoMachines supported by NIH 1S10RR23057 and the CNSI at UCLA. The authors also thank M. Murnane and J. Miao for encouragement and assistance in arranging the experiments.

References

- [1] S. Behyan, B. Haines, C. Karanukaran, J. Wang, M. Obst, T. Tyliczszak, S. G. Urquhart, Surface Detec-

tion in a STXM Microscope, AIP Conference Proceedings 1365 (1) (2011) 184–187. doi:10.1063/1.3625335.

- [2] J. Vila-Comamala, K. Jefimovs, J. Raabe, T. Pilvi, R. H. Fink, M. Senoner, A. Maaßdorf, M. Ritala, C. David, Advanced thin film technology for ultrahigh resolution X-ray microscopy, Ultramicroscopy 109 (11) (2009) 1360–1364. doi:10.1016/j.ultramic.2009.07.005. URL <http://www.sciencedirect.com/science/article/pii/S0304399109001661>
- [3] M. Obst, G. Schmid, 3d chemical mapping: application of scanning transmission (soft) X-ray microscopy (STXM) in combination with angle-scan tomography in bio-, geo-, and environmental sciences, Methods in Molecular Biology (Clifton, N.J.) 1117 (2014) 757–781. doi:10.1007/978-1-62703-776-1_34.
- [4] E. G. Rightor, A. P. Hitchcock, H. Ade, R. D. Leapman, S. G. Urquhart, A. P. Smith, G. Mitchell, D. Fischer, H. J. Shin, T. Warwick, Spectromicroscopy of Poly(ethylene terephthalate): Comparison of Spectra and Radiation Damage Rates in X-ray Absorption and Electron Energy Loss, The Journal of Physical Chemistry B 101 (11) (1997) 1950–1960, publisher: American Chemical Society. doi:10.1021/jp9622748. URL <https://doi.org/10.1021/jp9622748>
- [5] A. F. G. Leontowich, A. P. Hitchcock, R. F. Egerton, Radiation damage yields across the carbon 1s excitation edge, Journal of Electron Spectroscopy and Related Phenomena 206 (2016) 58–64. doi:10.1016/j.elspec.2015.11.010. URL <http://www.sciencedirect.com/science/article/pii/S0368204815002844>
- [6] J. Kirz, C. Jacobsen, M. Howells, Soft X-ray microscopes and their biological applications, Quarterly Reviews of Biophysics 28 (1) (1995) 33–130. doi:10.1017/S0033583500003139. URL <https://www.cambridge.org/core/journals/quarterly-reviews-of-biophysics/article/soft-xray-microscopes-and-their-biological-applications/23BB8B16B05396A85B4773993620222A>
- [7] K. Shinohara, T. Ohgashi, S. Toné, M. Kado, A. Ito, Quantitative analysis of mammalian chromosome by scanning transmission soft X-ray microscopy, Ultramicroscopy 194 (2018) 1–6. doi:10.1016/j.ultramic.2018.07.001. URL <http://www.sciencedirect.com/science/article/pii/S0304399117304126>
- [8] K. Litzius, I. Lemesch, B. Krüger, P. Bassirian, L. Caretta, K. Richter, F. Büttner, K. Sato, O. A. Tretiakov, J. Förster, R. M. Reeve, M. Weigand, I. Bykova, H. Stoll, G. Schütz, G. S. D. Beach, M. Kläui, Skyrmion Hall effect revealed by direct time-resolved X-ray microscopy, Nature Physics 13 (2) (2017) 170–175, number: 2 Publisher: Nature Publishing Group. doi:10.1038/nphys4000. URL <https://www.nature.com/articles/nphys4000>
- [9] X. Ye, J. E. Schmidt, R.-P. Wang, I. K. v. Ravenhorst, R. Oord, T. Chen, F. d. Groot, F. Meirer, B. M. Weckhuysen, Deactivation of Cu-Exchanged Automotive-Emission NH₃-SCR Catalysts Elucidated with Nanoscale Resolution Using Scanning Transmission X-ray Microscopy, Angewandte Chemie 132 (36) (2020) 15740–15747, eprint: <https://onlinelibrary.wiley.com/doi/pdf/10.1002/ange.201916554>. doi:<https://doi.org/10.1002/ange.201916554>.

- 462 URL <https://onlinelibrary.wiley.com/doi/abs/10.1002/ange.201916554> 527
- 463 1002/ange.201916554 528
- 464 [10] W. Li, Z. Wang, F. Zhao, M. Li, X. Gao, Y. Zhao, 529
- 465 J. Wang, J. Zhou, Y. Hu, Q. Xiao, X. Cui, M. J. 530
- 466 Eslamibidgoli, M. H. Eikerling, R. Li, F. Brandys, 531
- 467 R. Divigalpitiya, T.-K. Sham, X. Sun, Phosphorene 532
- 468 Degradation: Visualization and Quantification of 533
- 469 Nanoscale Phase Evolution by Scanning Transmission 534
- 470 X-ray Microscopy, *Chemistry of Materials* 32 (3) 535
- 471 (2020) 1272–1280, publisher: American Chemical 536
- 472 Society. doi:10.1021/acs.chemmater.9b04811. 537
- 473 URL <https://doi.org/10.1021/acs.chemmater.9b04811> 538
- 474 9b04811 539
- 475 [11] O. F. Vyvenko, T. Buonassisi, A. A. Istratov, 540
- 476 H. Hieslmair, A. C. Thompson, R. Schindler, E. R. 541
- 477 Weber, X-ray beam induced current—a synchrotron 542
- 478 radiation based technique for the in situ analysis of 543
- 479 recombination properties and chemical nature of metal 544
- 480 clusters in silicon, *Journal of Applied Physics* 91 (6) 545
- 481 (2002) 3614–3617. doi:10.1063/1.1450026. 546
- 482 URL <https://aip.scitation.org/doi/10.1063/1.1450026> 547
- 483 1450026 548
- 484 [12] B. Watts, D. Queen, A. L. D. Kilcoyne, T. Tylliszczak, 549
- 485 F. Hellman, H. Ade, Soft X-ray beam induced current 550
- 486 technique, *Journal of Physics: Conference Series* 186 551
- 487 (2009) 012023. doi:10.1088/1742-6596/186/1/012023. 552
- 488 URL <http://stacks.iop.org/1742-6596/186/i=1/a=012023?key=crossref.fbb9c0bc6b46433b2dbf69bf2007e655> 553
- 489 fbb9c0bc6b46433b2dbf69bf2007e655 554
- 490 555
- 491 [13] D. P. Bernstein, B. Bräuer, R. Kukreja, J. Stöhr, 556
- 492 T. Hauet, J. Cucchiara, S. Mangin, J. A. Katine, 557
- 493 T. Tylliszczak, K. W. Chou, Y. Acremann, Nonuni- 558
- 494 form switching of the perpendicular magnetization in 559
- 495 a spin-torque-driven magnetic nanopillar, *Physical Re- 560*
- 496 view B 83 (18) (2011) 180410. doi:10.1103/PhysRevB. 561
- 497 83.180410. 562
- 498 URL <https://link.aps.org/doi/10.1103/PhysRevB.83.180410> 563
- 499 83.180410 564
- 500 [14] A. Koehl, H. Wasmund, A. Herpers, P. Guttmann, 565
- 501 S. Werner, K. Henzler, H. Du, J. Mayer, R. Waser, 566
- 502 R. Dittmann, Evidence for multifilamentary valence 567
- 503 changes in resistive switching SrTiO₃ devices detected 568
- 504 by transmission X-ray microscopy, *APL Materials* 1 (4) 569
- 505 (2013) 042102. doi:10.1063/1.4822438. 570
- 506 URL <https://aip.scitation.org/doi/10.1063/1.4822438> 571
- 507 4822438 572
- 508 [15] J. Lim, Y. Li, D. H. Alsem, H. So, S. C. Lee, P. Bai, 573
- 509 D. A. Cogswell, X. Liu, N. Jin, Y.-s. Yu, N. J. Salmon, 574
- 510 D. A. Shapiro, M. Z. Bazant, T. Tylliszczak, W. C. 575
- 511 Chueh, Origin and hysteresis of lithium compositional 576
- 512 spatiodynamics within battery primary particles, *Science* 577
- 513 353 (6299) (2016) 566–571. doi:10.1126/science.aaf4914. 578
- 514 aaf4914. 579
- 515 URL <https://science.sciencemag.org/content/353/6299/566> 580
- 516 6299/566 581
- 517 [16] A. Erbil, G. S. Cargill III, R. Frahm, R. F. Boehme, 582
- 518 Total-electron-yield current measurements for near- 583
- 519 surface extended x-ray-absorption fine structure, *Physical Review B* 37 (5) (1988) 2450–2464. doi:10.1103/PhysRevB.37.2450. 584
- 520 37.2450. 585
- 521 URL <https://link.aps.org/doi/10.1103/PhysRevB.37.2450> 586
- 522 37.2450 587
- 523 [17] G. B. Kim, H. J. Song, H. J. Shin, C. K. Hong, X-ray 588
- 524 absorption spectroscopy in total electron yield mode of 589
- 525 scanning photoelectron microscopy, *Journal of Electron 590*
- 526 Spectroscopy and Related Phenomena 148 (3) (2005) 591
- 137–141. doi:10.1016/j.elspec.2005.04.005.
- [18] B. H. Frazer, B. Gilbert, B. R. Sonderegger, 592
- G. De Stasio, The probing depth of total electron 593
- yield in the sub-keV range: TEY-XAS and 594
- X-PEEM, *Surface Science* 537 (1-3) (2003) 161–167. 595
- doi:10.1016/S0039-6028(03)00613-7. 596
- URL <http://linkinghub.elsevier.com/retrieve/pii/S0039602803006137> 597
- [19] M. Stuckelberger, B. West, T. Nietzold, B. Lai, J. M. 598
- Maser, V. Rose, M. I. Bertoni, Engineering solar 599
- cells based on correlative X-ray microscopy, *Journal 600*
- of Materials Research 32 (10) (2017) 1825–1854. 601
- doi:10.1557/jmr.2017.108. 602
- URL https://www.cambridge.org/core/product/identifier/S088429141700108X/type/journal_article 603
- [20] L. Chayanun, V. Dagytė, A. Troian, D. Salomon, 604
- M. Borgström, J. Wallentin, Spectrally resolved x-ray 605
- beam induced current in a single InGaP nanowire, 606
- Nanotechnology* 29 (45) (2018) 454001. doi:10.1088/ 607
- 1361-6528/aadc76. 608
- [21] T. E. Everhart, O. C. Wells, R. K. Matta, A novel 609
- method of semiconductor device measurements, 610
- Proceedings of the IEEE* 52 (12) (1964) 1642–1647. doi: 611
- 10.1109/PROC.1964.3460. 612
- [22] H. J. Leamy, Charge collection scanning electron mi- 613
- croscopy, *Journal of Applied Physics* 53 (6) (1982) 614
- R51–R80. doi:10.1063/1.331667. 615
- URL <http://aip.scitation.org/doi/abs/10.1063/1.331667> 616
- [23] W. A. Hubbard, M. Mecklenburg, H. L. Chan, 617
- B. C. Regan, STEM Imaging with Beam-Induced 618
- Hole and Secondary Electron Currents, *Physical 619*
- Review Applied* 10 (4) (2018) 044066. 620
- doi:10.1103/PhysRevApplied.10.044066. 621
- URL <https://link.aps.org/doi/10.1103/PhysRevApplied.10.044066> 622
- [24] M. Mecklenburg, W. A. Hubbard, J. J. Lodico, B. C. 623
- Regan, Electron beam-induced current imaging with 624
- two-angstrom resolution, *Ultramicroscopy* 207 (2019) 625
112852. doi:10.1016/j.ultramic.2019.112852. 626
- URL <http://www.sciencedirect.com/science/article/pii/S0304399119302311> 627
- [25] W. A. Hubbard, Z. Lingley, J. Theiss, S. Sitzman, 628
- T. Ayvazian, M. Brodie, B. Foran, Scanning trans- 629
- mission electron microscope mapping of electronic 630
- transport in polycrystalline BaTiO₃ ceramic capaci- 631
- tors, *Applied Physics Letters* 115 (13) (2019) 133502. 632
- doi:10.1063/1.5117055. 633
- URL <http://aip.scitation.org/doi/10.1063/1.5117055> 634
- [26] J. Maser, C. Jacobsen, J. Kirz, A. Osanna, S. Spec- 635
- tor, S. Wang, J. Warnking, Development of a Cryo 636
- Scanning Transmission X-Ray Microscope at the NSLS, 637
- in: J. Thieme, G. Schmahl, D. Rudolph, E. Umbach 638
- (Eds.), *X-Ray Microscopy and Spectromicroscopy: 639*
- Status Report from the Fifth International Confer- 640
- ence, Würzburg, August 19–23, 1996, Springer, 641
- Berlin, Heidelberg, 1998, pp. 35–44. doi:10.1007/ 642
- 978-3-642-72106-9_4. 643
- URL https://doi.org/10.1007/978-3-642-72106-9_4 644
- [27] D. A. Shapiro, R. Celestre, B. Enders, J. Joseph, 645
- H. Krishnan, M. A. Marcus, K. Nowrouzi, H. Pad-

592 more, J. Park, A. Warwick, Y.-S. Yu, The COSMIC
593 Imaging Beamline at the Advanced Light Source: a
594 new facility for spectro-microscopy of nano-materials,
595 Microscopy and Microanalysis 24 (S2) (2018) 8–11.
596 doi:10.1017/S1431927618012485.

597 [28] P. Denes, D. Doering, H. A. Padmore, J.-P. Walder,
598 J. Weizeorick, A fast, direct x-ray detection charge-
599 coupled device, Review of Scientific Instruments 80 (8)
600 (2009) 083302. doi:10.1063/1.3187222.
601 URL [http://aip.scitation.org/doi/10.1063/1.](http://aip.scitation.org/doi/10.1063/1.3187222)
602 [3187222](http://aip.scitation.org/doi/10.1063/1.3187222)

603 [29] S. Marchesini, H. Krishnan, B. J. Daurer, D. A.
604 Shapiro, T. Perciano, J. A. Sethian, F. R. N. C. Maia,
605 SHARP: a distributed GPU-based ptychographic
606 solver, Journal of Applied Crystallography 49 (4) (2016)
607 1245–1252, number: 4 Publisher: International Union
608 of Crystallography. doi:10.1107/S1600576716008074.
609 URL [http://scripts.iucr.org/cgi-bin/paper?](http://scripts.iucr.org/cgi-bin/paper?jo5020)
610 [jo5020](http://scripts.iucr.org/cgi-bin/paper?jo5020)